Journal of Alloys and Compounds 770 (2019) 710–720

Contents lists available at ScienceDirect

Journal of Alloys and Compounds

journal homepage: http://www.elsevier.com/locate/jalcom

Conductive $CaSi_2$ transparent in the near infra-red range

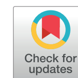

Nikolay G. Galkin [a,*], Sergey A. Dotsenko [a], Konstantin N. Galkin [a], Andrey M. Maslov [a], Dmitrii B. Migas [c], Vlodislav O. Bogorodz [b], Andrey B. Filonov [b], Victor E. Borisenko [b], Ildiko Cora [c], Bela Pécz [c], Dmitrii L. Goroshko [a], Andrei V. Tupkalo [a], Evgenii A. Chusovitin [a], Evgenii Y. Subbotin [a]

[a] *Laboratory of Optics and Electrophysics, Institute of Automation and Control Processes, Far Eastern Branch of Russian Academy of Sciences, Radio Str. 5, 690041, Vladivostok, Russia*

[b] *Department of Micro- and Nanoelectronics, Belarusian State University of Informatics and Radioelectronics, P. Browka 6, 220013, Minsk, Belarus*

[c] *Department of Thin Layer Physics, Institute of Technical Physics and Materials Research, Centre for Energy Research, Hungarian Academy of Sciences, 1525, Budapest Pf, 49, Hungary*

A R T I C L E I N F O

Article history:
Received 21 February 2018
Received in revised form
28 July 2018
Accepted 18 August 2018
Available online 20 August 2018

Keywords:
Calcium disilicide
Double heterostructures
Ab initio calculations
Electronic band structure
Optical and transport properties
A gap-less semiconductor
Infra-red transparency

A B S T R A C T

The methods of heteroepitaxial growth of $Si/CaSi_2/Si(111)$ double heterostructures (DHS) at 500 °C have been developed. Thin $CaSi_2$ layers with the thicknesses of 14–40 nm have been successfully embedded in the silicon matrix. The $hR6\text{-}CaSi_2(001)||Si(111)$ with $hR6\text{-}CaSi_2[100]||Si[1\bar{1}0]$ epitaxial relationship has been conserved for the embedded $CaSi_2$ layer regardless of its thickness and the Si overgrowth mode (molecular beam epitaxy or solid phase epitaxy). The embedded $CaSi_2$ layers are characterized by the lattice parameter distortion of about ±4% due to the difference in the thermal expansion coefficients of the silicide and silicon. Two types of Si overgrowth atop $CaSi_2(001)$ planes have been observed: (i) {111}-twinned Si crystals were found onto the $CaSi_2(001)$ surface in the DHS with $CaSi_2$ thickness of 32–40 nm, which have preserved the {111} planes parallel to the Si(111) ones of the substrate; (ii) a polycrystalline twinned Si capping layer with a variable thickness has been formed in the samples with the smallest $CaSi_2$ thickness (14–16 nm). Experimentally determined optical functions for the $CaSi_2$ layer embedded in the silicon matrix have shown the presence of degenerate semiconducting properties with strong absorbance at the photon energies higher than 2.3 eV and small contribution from the free carrier absorption at 0.4–1.2 eV. *Ab initio* calculations within the generalized gradient approximation and screened hybrid functional of the hR-6 $CaSi_2$ bulk with and without lattice distortion (by ±3%) have demonstrated the metal or gapless semiconductor energy band structure, because the Fermi level crosses several bands also assuming a huge free carrier concentration. The low-temperature Hall measurements and magnetoresistance measurements have proved that $CaSi_2$ films on silicon are a gapless semiconductor with two types of carrier "pockets" (holes and electrons) that determine the resulting conductivity, concentration and mobility as a function of the Fermi level shift with the temperature increase. Mechanisms of the experimentally observed optical transparency of $CaSi_2$ in the infra-red range are discussed.

© 2018 Elsevier B.V. All rights reserved.

1. Introduction

Both metal and semiconducting silicides are well known to be fully compatible with common silicon technologies and often used in microelectronics [1,2]. Even though transition metal silicides were mainly investigated in the past [1,2], nowadays alkaline-earth silicides started gaining much attention [3,4] also owing to interesting properties as thin films and 2D-like materials [5]. Two semiconducting silicides are usually mentioned to be formed in the Ca-Si system: Ca_2Si [3,6,7] and Ca_3Si_4 [8,9]. The first one is synthesized in the bulk and thin layer forms. According to *ab initio* calculations it has the band gap of 1.02 eV within the GW approximation [6] and 0.35 eV within the local density approximation (LDA) [3]. The second silicide has been fabricated only as a bulk sample by hot pressing of Ca and Si powders [9]. Its band gap is not known except for the theoretical predictions of 0.35 eV [8] and 0.598 eV [10].

* Corresponding author.
E-mail address: ngalk@iacp.dvo.ru (N.G. Galkin).

https://doi.org/10.1016/j.jallcom.2018.08.179
0925-8388/© 2018 Elsevier B.V. All rights reserved.

Meanwhile, $CaSi_2$ can be viewed as a compound in the Ca-Si system with the largest silicon content [9]. Its crystal structure depends on the external pressure. In fact, at an atmospheric pressure it has a rhombohedral lattice of the R-3m space group existing in two hR3 and hR6 modifications [11–13] with one Ca and two Si chemically inequivalent sites [11]. At the pressure of 5.7 GPa and temperature of 510 °C it transforms into the tetragonal lattice of the *I41/amd* space group [11–13].

Crystalline $CaSi_2$ layers can be epitaxially grown on Si(111) by room temperature deposition of this material and subsequent high temperature annealing [14] or by reactive diffusion supposing deposition of Ca atoms onto Si substrate heated to 700–900 °C [15]. The last approach is usually referred to as a reactive deposition (RD) technique. In both cases the hR6 phase forms first [14,15] then it transforms into the final hR3 one when the thickness of the layer reaches 200 nm [15].

Theoretical investigations of electronic and optical properties of $CaSi_2$ [11,16] have pointed out this silicide to behave like a metal. At the same time existing experimental data of such epitaxial layers are quite contradicting. Thick $CaSi_2$ layers are found to have electronic properties of a compensated metal [14] for which electrons and holes with different effective masses and concentrations up to 2×10^{21} cm^{-3} contribute in an equivalent way to the conductivity [17]. There is a weak temperature dependence of the $CaSi_2$ conductivity registered in the bulk and thin layer samples. It is explained by different temperature dependences of hole and electron mobilities along with a change in the carrier's sign from negative (electrons) to positive (holes) at the temperature of about 200 K [17]. From the other side, strong direct interband transitions with the energies of 0.89 eV and 0.912 eV [18,19] and the photoluminescence peak at about 0.95 eV at 5 K [20] observed in the polycrystalline $CaSi_2$ layers formed by RD method on Si(111) substrates at markedly lower temperature (500 °C) do not witness this silicide to be a metal or semimetal. Meanwhile, experimentally determined transparency in the photon energy range of 0.2–0.7 eV, the energy band gap of 0.63 eV and a plasma reflection at the energies less than 0.2 eV [19,20] are more typical for a degenerate semiconductor than for a compensated metal [14]. However, in Refs. 19 and 20 the crystal structure of the grown silicide was not exactly determined. Meanwhile, electrically conducting materials with high optical transparency are of great practical importance.

In order to resolve the above contradictions we fabricated Si/$CaSi_2$/Si(111) and $CaSi_2$/Si(111) epitaxial heterostructures and studied their electronic, optical and electrical properties combining experimental measurements with first principle calculations. The results are presented in this paper.

2. Experimental procedure

Si/$CaSi_2$/Si(111) heterostructures were grown in the ultra-high vacuum "VARIAN" chamber with the base pressure of 2×10^{-10} Torr. The chamber had Auger electron spectroscopy (AES) and electron energy loss spectroscopy (EELS) facilities. Rectangular monocrystalline stripes of *p*-type Si(111) with the dimensions of 5×18 mm^2 and conductivity of 45 Ω cm were used as substrates and Si sublimation sources.

Atomically clean surface of Si(111) was formed by thermal flashing at 1250 °C in the vacuum chamber. The surface purity was controlled by AES and EELS. In all experiments Ca and Si deposition rates were controlled by a quartz sensor. In all growth experiments the Ca atoms were deposited at the rate $\upsilon_{Ca} = (1.0$ and $2.0)$ nm/min onto clean Si(111)7 × 7 surface at 500 °C. Then Si capping layer as thick as 50 nm was deposited at $\upsilon_{Si} = 2.0$ nm/min at the same temperature (molecular beam epitaxy (MBE) mode) or at room temperature with subsequent annealing in vacuum at 500 °C (solid phase epitaxy (SPE) mode). In both modes Si/$CaSi_2$/Si(111) double heterostructures (DHSs) were formed. Their fabrication parameters are summarized in Table 1. Moreover, one sample (sample *E*) was fabricated with the silicide thicker than others and without a capping layer.

Cross-sections of the samples thinned by the procedure presented in Ref. [21] were analyzed with a high resolution transmission electron microscopy (HRTEM) in Philips CM 20 and JEOL 3010 HR microscopes. The latter was equipped with an energy filtering attachment (EFTEM). Selected area electron diffraction (SAED) and selected area fast Fourier transformations (SAFFT) of HRTEM images were used to study epitaxial relationships in the fabricated structures. SingleCrystalTM and CrystalMaker® software [22] was employed for that. Surface morphology was analyzed by atomic force microscopy (AFM) with the use of "Calculating of Average Parameters of Objects on Surface" software [23].

Optical reflectance (*R*-spectra) and transmittance (*T*-spectra) of the samples were recorded at room temperature in the photon energy range of 0.05–6.20 eV in Hitachi U-3010 spectrophotometer and Bruker Vertex 80v Fourier spectrometer. Raman spectra exited by the light with the wavelength of 488 nm were registered also at room temperature with "WITec alpha 300 RSA+" confocal Raman microscope (TP&MS HAS, Hungary). Hall effect and magnetoresistance measurements in the sample *E* were carried out in the temperature range 30–300 K on an automated Teslatron unit with a closed cooling circuit. Measurements of the Hall parameters of the sample are performed at a DC 10 μA in the magnetic field of 0.5 T. Magnetoresistance was measured at temperatures of 50 K, 120 K and 300 K versus magnetic field from 0 T to 4 T with sample current of 10 μA.

3. Computational details

The full structural optimization of the $CaSi_2$ bulk has been performed by employing the first principles total energy projector-augmented wave method (code VASP) [24–27]. Both the generalized gradient approximation (GGA) of Perdew-Burke-Ernzerhof [28] and screened hybrid functional of Heyd, Scuseria, and Ernzerhof (HSE) with the standard settings for the screening and Hartree Fock mixing parameters [29–33] were used. Our calculations have been performed by implementing the energy cutoff of 320 eV and $13 \times 13 \times 9$ (for GGA) and $6 \times 6 \times 2$ (for HSE) grids of Monkhorst-Pack points. Structural optimization was stopped when forces acting on the atoms were smaller than 0.01 eV/Å. The convergence in the total energy was better than 1meV/atom.

The electronic band structures and optical functions have also been calculated by the self-consistent means of the self-consistent full potential linearized augmented plane wave (FLAPW) method in its scalar-relativistic version using WIEN2k package [34]. The structural parameters of the $CaSi_2$ bulk fully optimized by the projector-augmented wave method have been taken into consideration. We also applied GGA of Perdew-Burke-Ernzerhof [28] and the screened hybrid functional YS-PBE0 (which is similar to HSE)

Table 1
Fabrication parameters of double heterostructure Si/$CaSi_2$/Si(111) (*A-D*) and single heterostructures $CaSi_2$/Si(111) (*E*).

Samples	Ca thickness, nm	Average silicide thickness, Nm	The mode of top Si layer growth
A	36	40	MBE
B	16	16	MBE
C	36	32	SPE
D	16	14	SPE
E	72	108	no

[35]. We performed the self-consistent procedure on grids of 85 k-points (GGA) and 28 k-points (YS-PBE0) in the irreducible part of the Brillouin zone. Further increase in the k-point number did not lead to any noticeable changes in the eigenvalues. The self-consistent procedure was continued until the difference between the total energies in two successive iterations was less than 1 meV/atom. Since the HSE calculations are very time consuming, the absorption coefficient and reflectivity have been estimated within GGA at a dense mesh of at least 781 k-points in the irreducible part of the corresponding Brillouin zone.

4. Results and discussion

4.1. Lattice parameters and defects in the Si/$CaSi_2$/Si(111) double heterostructures

The structure and epitaxial relationships in the fabricated DHSs are illustrated in Fig. 1. Epitaxial $CaSi_2$ is found to be formed independently of the amount of deposited Ca and Si overgrowth mode (SPE or MBE). The SAED patterns from DHS (inserts in Fig. 1a and b) have unambiguously proven the heteroepitaxial growth of $CaSi_2$ with hR6-$CaSi_2$ structure on the Si(111) substrate regardless of the Si overgrowth regime (SPE or MBE) and a non-abrupt $CaSi_2$/Si(111) interface. Besides, the inhomogeneity thickness in the $CaSi_2$ and Si capping layers was observed from both HRTEM data in the BF regimes (Fig. 1a and b) and in the DF regime (Fig. 1c) that correlated with the roughness value estimated by AFM for both samples [19,20]. The DF image was acquired with the 006 reflection of the hR6-type $CaSi_2$ phase. The $CaSi_2$ and Si capping layers in the DHS are clearly separated (Fig. 1a,c).

The thickness of the $CaSi_2$ layer in the sample *C* (Fig. 1a) was found to be 25–45 nm, while the thickness of the Si layer on the top varied from 60 nm to 30 nm (an average value of about 50 nm). The embedded $CaSi_2$ layer and this Si capping layer were not uniform in thickness that confirms a 3D island growth of the silicide and a non-uniform nucleation of Si atop the $CaSi_2$ layer. Direct observations have shown near 1.5 times decrease of the real $CaSi_2$ thickness (Fig. 1a, an average value of about 32 nm) starting from 54 nm, corresponding to 36 nm ($d_{CaSi2.} \approx 1.5 \times d_{Ca}$) of the deposited Ca layer as previously determined by the calibration procedure. An average $CaSi_2$ thickness in the sample *A* was about 40 nm (Fig. 1b and c).

The same feature was observed for the other DHSs (samples *B* and *D*, Table 1) with smaller $CaSi_2$ thicknesses (24 nm is expected while 14–17 nm is its real thickness by HRTEM data (not shown)) and different Si overgrowth modes. The reason for such a thickness reduction can be a decrease in the Ca calculated deposition rate due to a decrease of Ca mass in the evaporator. Additionally, the decrease of the Ca sticking coefficient to a silicon substrate at 500 °C must be taken into consideration. This leads to the overestimation of calculated thickness and to the increase of the experimental error in the determination of a real $CaSi_2$ layer thickness.

Investigations of the epitaxial relations and lattice parameters for DHSs were carried out by analyzing the HRTEM images and SAFFT patterns from different parts of DHSs, including interfaces, the $CaSi_2$ layer and the Si capping layer. HRTEM images for the sample *C* (Fig. 2a) and the sample *A* (Fig. 3a) with the largest Ca thickness (36 nm, Table 1) are shown. Different parts of the cross section were marked by white circles, from which SAFFT patterns (Figs. 2b and 3b) were recorded and then analyzed.

Additional analysis of the DHS and its SAFFT patterns has shown the nearly flat $CaSi_2$/Si(111) interface (sample *C*, Fig. 2a, the area 1) with hR6-$CaSi_2$[100]||Si [1$\bar{1}$0] and hR6-$CaSi_2$(001)||Si(111) epitaxial relationships. There were no stacking faults identified in a 3–4 unit cell thickness (Fig. 2 c). At larger distances from the Si(111) substrates several stacking faults of the Si sheets in the $CaSi_2$ structure and twins were found (Fig. 2c). At the Si/$CaSi_2$ interface the hR6-type $CaSi_2$ crystal (R-3m; $a = 0.393 \pm 0.002$ nm; $c = 3.09 \pm 0.18$ nm) in the [100] projection with stacking faults and the epitaxially grown {111}-twinned Si crystals (the area 4, Fig. 3 a) were found. Grains in Si top layer were epitaxially grown onto the $CaSi_2$(001) surface (and the Si(111) surface of the substrate, as well).

The epitaxial relationships for the $CaSi_2$(001) on Si(111) substrate and almost abrupt $CaSi_2$/Si(111) interface were conserved for DHSs with the MBE Si overgrowth (Fig. 3a, sample *A*, area 1). But some steps were observed on the Si/$CaSi_2$ interface for both DHSs by HRTEM data (Figs. 2a and 3a). This can be explained by the competition between bulk and surface diffusion of Ca and Si atoms in the formation of a continuous $CaSi_2$ layer.

The stacking sequence was analyzed using the HRTEM images for areas 2 and 3 (Fig. 3a). It was established (Fig. 3b) that in the first 5–10 nm thick part of the hR6-type $CaSi_2$ crystal (R-3m; $a = 0.382 \pm 0.002$ nm; $c = 3.09 \pm 0.18$ nm) a few stacking faults were observed (Fig. 3c). Afterwards $CaSi_2$ sheets were grown without faults. In the upper and thinner part of the Si capping layer the {111}-twinned Si grains were grown onto the $CaSi_2$(001) surface and the Si grains are still oriented (area 4, Fig. 3a), *i.e.* one of the {111} planes is parallel to the Si(111) of the substrate. Mainly the {111}-type twin boundaries and stacking faults are identified. The structural relationships and overlapping of the twinned Si grains are similar to the observations from the sample *C* (Fig. 2a,c).

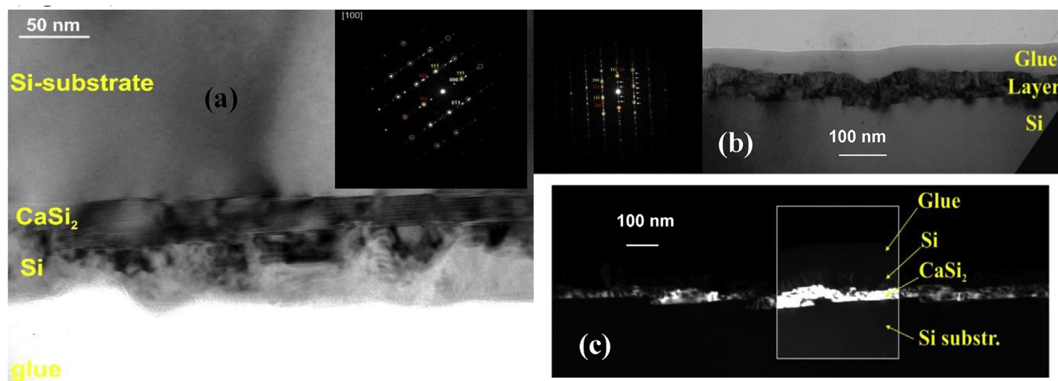

Fig. 1. HRTEM images and SAED patterns (inserts) for the Si/$CaSi_2$/Si(111) DHS with the Si grown in SPE ((a), sample *C*) and MBE ((b,c), sample *A*) modes. For sample *A* (b) bright field (BF) (b) and dark field (DF) (c) HTEM images of the Si and the thin layer on it. Inserts on (a) and (b) are SAED patterns for samples *C* and *A*, respectively.

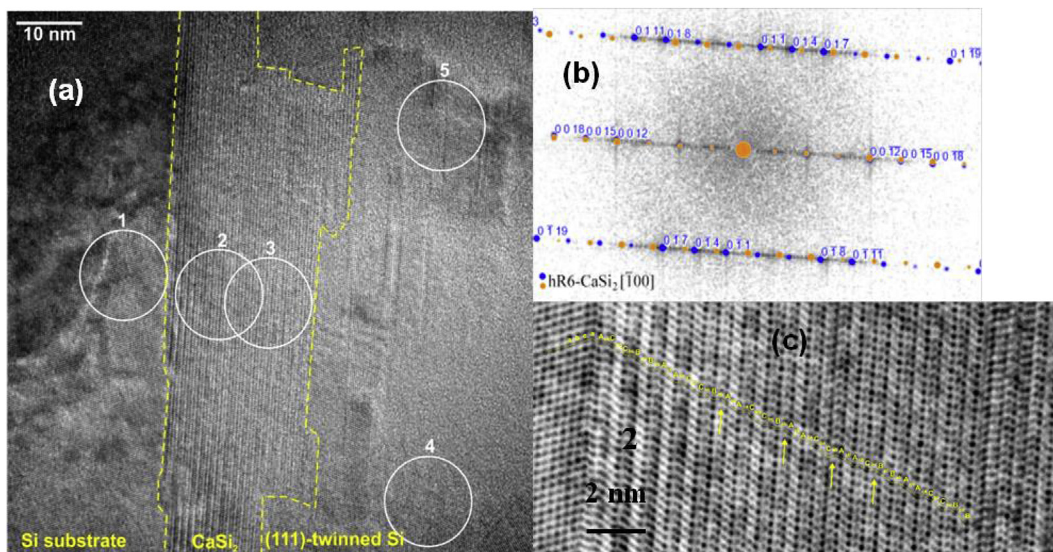

Fig. 2. (a) - HRTEM images taken from the Si/hR-6 $CaSi_2$/Si(111) DHSs with Si layers grown in SPE (sample *C*) mode with inserts of white circles from 1 to 5 distributed in the DHS with Si and $CaSi_2$ layers. SAFFT patterns from areas (2) in (b) with identification for $CaSi_2$ planes in DHS with SPE. (c) - HRTEM image of the interface and the hR6-type $CaSi_2$ in the area 2. Densities on the image is inverted (i.e. dark spots correspond to atoms/groups of atoms). Stacking sequence of the hR6-type $CaSi_2$ is indicated in ~5 unit cell thickness. A few stacking faults of the Si sheet in the $CaSi_2$ structure are indicated by yellow arrows. (For interpretation of the references to colour in this figure legend, the reader is referred to the Web version of this article.)

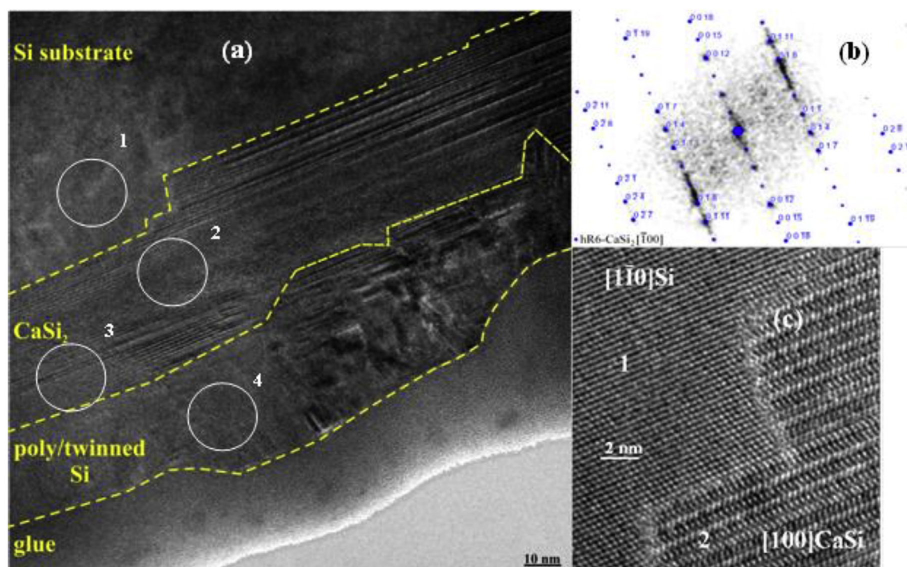

Fig. 3. (a) - HRTEM images taken from the Si/hR-6 $CaSi_2$/Si(111) DHS with Si layers grown by MBE mode (sample *A*) with inserts of white circles from 1 to 4 distributed in the DHS with Si and $CaSi_2$ layers. SAFFT patterns from areas (2) in (b) with identification for $CaSi_2$ planes in DHS with MBE Si growth mode. (c) - HRTEM image of the $CaSi_2$/Si(111) interface in the region between 1 and 2 areas on (a).

A thorough analysis of the SAFFT patterns (Figs. 2(b) and 3(b)) from the cross-sectional patterns of DHSs (samples *A* and *C*) has shown that there are different deviations (stretching on 0.27–4.58% and compression on 0.5–3.2%, Table 2) from tabular values for the $CaSi_2$ planes [11,15,36] in the $CaSi_2$ [ī00] direction. Simultaneously, 0.22–1.04% compression and 0.33–0.54% stretching were observed in the silicon lattice near the Si/$CaSi_2$ interface (Table 3) that related to the difference in the lattice parameters [14] at the growth and room temperatures.

The {111}-twined Si layers were grown on the $CaSi_2$(001) surface for all studied samples with Ca calibrated thicknesses of 16 nm and 36 nm. They conserve the parallel plane to the (111) plane of the Si substrate. Mainly the {111}-type twin boundaries and stacking faults were identified. The structural relationships and overlapping of the twinned Si grains are similar to the observations for *A*, *B*, *C* and *D* samples. These epitaxial correlations were conserved for the embedded $CaSi_2$ layers regardless of their actual thickness and the Si overgrowth mode. Cross-sections of all grown DHSs demonstrate sharp epitaxial interfaces: $CaSi_2$ (001)//Si(111) and $CaSi_2$[ī00]//Si [1ī0] with the formation of the embedded thin hR6 $CaSi_2$ crystal in Si. However, the crystalline quality and thickness uniformity of the capping silicon layer were inferior for the DHSs with small $CaSi_2$ thicknesses. So, a polycrystalline Si twinned layer with variable thickness is formed in the samples with the smallest $CaSi_2$

Table 2
Identifications of $CaSi_2$ planes in [ī00] direction on SAFFT patterns for samples *A* and *C* with Si/hR6 $CaSi_2$/Si(111) DHSs.

Planes in $CaSi_2$[ī00] direction	d_{CaSi2}(tab) [36], nm	d_{CaSi2} (sample *C*), nm	d_{CaSi2} (sample *A*), nm	Intensity [36], %	$\Delta d/d$, (sample *C*) %	$\Delta d/d$, (sample *A*)%
$CaSi_2$(006)	0.5102	0.511	0.520	1.86	0.24	1.96
$CaSi_2$(009)	0.3403	0.329	0.338	0.65	−3.35	−0.79
$CaSi_2$(00 12)	0.2551	0.258	0.258	62.66	1.10	1.02
$CaSi_2$(01-1)	0.3323	0.338	0.329	25.55	1.84	−1.05
$CaSi_2$(01-4)	0.3053	0.310	0.320	43.39	1.54	4.91
$CaSi_2$(01-7)	0.2555	0.269	0.261	100	5.13	2.11
$CaSi_2$(018)	0.2517	0.256	0.251	43.13	1.83	−0.40
$CaSi_2$(01 11)	0.2138	0.217	0.213	57.33	1.40	−0.51

Table 3
Identifications of the Si planes in the Si [1ī0] direction on the SAFFT pattern for samples with the Si/$CaSi_2$/Si(111) DHSs.

Planes in Si [1ī0] direction	d_{Si}(tab), nm	d_{Si} (sample *C*), nm	d_{Si} (sample *A*), nm	$\Delta d/d$, (Sample *C*) %	$\Delta d/d$, (sample *A*)%
Si(002)	0.2715	0.273	0.271	0.54	−0.11
Si(111)	0.31356	0.313	0.315	−0.28	0.33
Si(220)	0.19201	0.192	0.190	−0.22	−1.05

thicknesses (samples *B* and *D*).

Calculations of the lattice parameters for the embedded $CaSi_2$ layers in both DHSs have shown (Table 4) that the rhombohedral R-3m $CaSi_2$ structure with the hR6 modification has the closest values (with deviation in unit of percent) of the interplanar distances to the tabular R-3m $CaSi_2$ ones [36] and their reflex's intensity. Therefore, it can be concluded that the grown DHSs have $CaSi_2$ composition with the R-3m structure and hR6 modification, but not Ca_3Si_4 as we previously supposed [18–20].

The fully optimized lattice parameters of $CaSi_2$ in the hR6 modification by the projector-augmented wave method [36] in comparison with the experimentally determined ones are summarized in Table 4. A very good agreement is evident. Moreover, the optimization of lattice parameters has been done at zero temperature and the corresponding thermal lattice expansion coefficients should be considered that leads to even more perfect match of theoretical to experimental data.

4.2. Experimental optical spectra of $CaSi_2$/Si(111) single and Si/$CaSi_2$/Si(111) double heterostructures

Transmittance (T) and reflectance (R) spectra of the *C* and *D* samples are presented in Fig. 4 for comparison. Well-pronounced maximum in R-spectra at 0.8 eV is evident for the both DHS samples. The sample *E* with thick $CaSi_2$ layer displays almost the same behavior. The transmittance of DHS samples in the photon energy range of 0.6–1.0 eV is high enough (0.4–0.5). It is comparable to Si substrate transmittance (0.50–0.52, not shown in Fig. 4a).

At photon energies smaller than 0.4 eV the strong decrease in the transmittance is caused by absorbance along with an increase of reflectance (Fig. 4b). Such a behavior can correspond to the plasma resonance on free carriers [37]. Since non-doped Si was used as a sublimation source for the Si capping layer, the latter did not have a large concentration of free carriers. Therefore, free carries can appear only in the embedded $CaSi_2$ layer. It has been confirmed by small resistivity of the sample *E*, which is slowly decreasing with a temperature decrease [18].

The same *R*- and *T*-spectra character were previously observed for the MBE grown DHS sample *A* (Table 1) with the embedded silicide layer of 40 nm [20] indicating the presence of the plasma resonance on free carriers in the layer to be independent of the mode of the Si overgrowth (MBE or SPE). The energy position of plasma resonance on free carriers in the *R*-spectrum shows the blue shift (0.05–0.12 eV) at the free carrier concentration increase from 10^{19} cm^{-3} to 10^{21} cm^{-3} [37].

The known lowest coefficients of reflection of different semiconductors and semimetals are 0.1–0.2 at 0.01–0.1 eV [3,38,39]. But in our study the 0.37–0.41 eV values were registered for the samples *C* and *D* (Fig. 4b). Such a behavior can be explained by the zero absorbance in the Si substrate and an increase of the measured reflection coefficient due to multiple reflections from the substrate. Thus, the measured reflectance spectrum in the energy range of 0.4–1.0 eV does not fully stem from the plasma resonance effect in semiconductors.

We have used the Kukharskii-Subashiev fitting procedure for one type of charge carriers in a heavily doped semiconductor [40]. The calculated reflection coefficient did not coincide with the one extracted from the experimental *R*-spectrum. The second possible reason is the contribution of two charge carrier types in the plasma resonance with strongly different effective masses in accordance with theoretical [11] and experimental [17] results.

In spite of the grown Si top layer, near the same high energy level, the reflectance peaks (0.9–1.0, 1.3–1.7, 2.0–2.6 and 3.7–3.8 eV) were observed in the $CaSi_2$/Si(111) heterostructure (sample *E*, Fig. 4a) and Si/$CaSi_2$/Si(111) DHSs grown by MBE [20] and SPE (Fig. 4b). Since the intensities of peaks at 4.5 and 5.5 eV, corresponding to Si, are slightly decreased, we consider the Si capping layer to have a poorer crystalline quality than the Si substrate. But comparing the widths of the mentioned Si peaks one can suppose that the crystalline quality of the Si capping layer is better for the sample *C* with larger $CaSi_2$ thickness. In the low photon energy range (0.6–1.2 eV) the measured reflectance of Si/$CaSi_2$/Si(111) DHSs (samples *C* and *D*) and $CaSi_2$/Si(111) heterostructure (sample *E*) is mainly determined by contribution of the Si substrate due to

Table 4
Calculated parameters of hR6-$CaSi_2$ lattice in the [ī00] direction.

$CaSi_2$ lattice parameters, nm	Sample *C*	Sample *A*	Bulk [36]	$\Delta d/d$, (sample *C*) %	$\Delta d/d$, (sample *A*) %	Data errors, %	GGA	HSE
a	0.393	0.382	0.386	1.84	−1.09	±0.56	0.3877	0.3858
c	3.09	3.09	3.06	1.14	1.07	±6.0	3.0341	3.0405

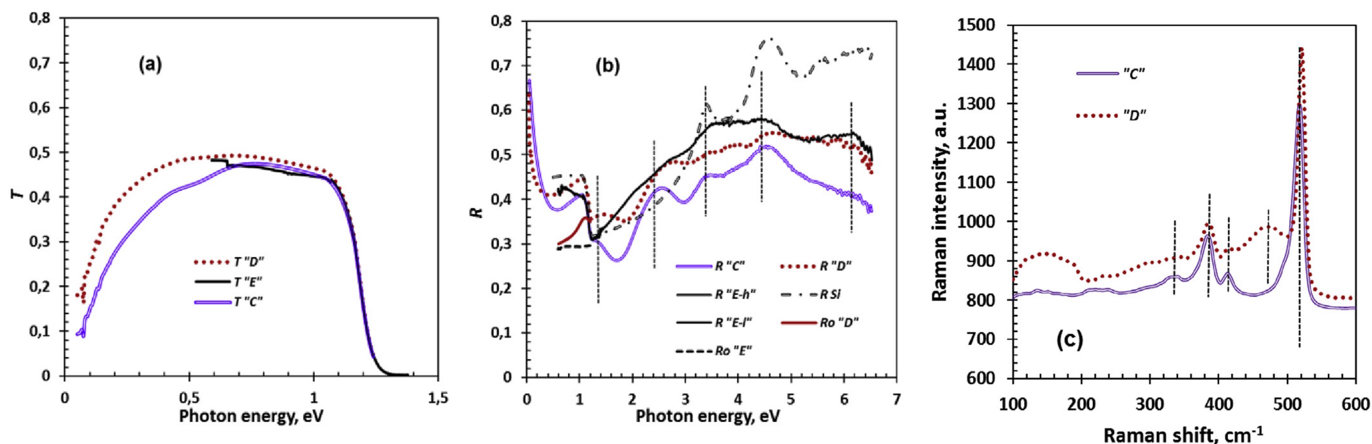

Fig. 4. (a) - Transmittance (*T*) and (b) - reflectance (*R*) spectra of Si/$CaSi_2$/Si(111) (samples *C* and *D*) double heterostructures, $CaSi_2$/Si(111) heterostructure (sample *E*) and Si substrate. Curves R_o"*D*" and R_o"*E*" are reflectance spectra of samples *D* and *E* in the photon energy range of 0.3–1.2 eV calculated in the frame of two-layer model [41] for $CaSi_2$ layer from experimental *R*-spectra. (c) Raman spectra of DHSs (samples *C* and *D*). The notations *R "E-l"* and *R "E-h"* are associated with low-energy (0.6–1.2 eV) and high-energy (1.2–6.5 eV) measurements of the reflection coefficients for the sample *E*.

its transmittance and the light reflectance from the back side. Thus, for the calculation of real reflection coefficient of the layer (R_o) we used the two-layer model called RT-procedure [41], which includes the multiple reflections in the layer and substrate. Calculated values for samples *D* and *E* are presented in Fig. 4b (curves R_o"*D*" and R_o"*E*").

The phonon structure of the $CaSi_2$ layers with different thicknesses capped by SPE silicon characterized by the Raman spectroscopy is presented in Fig. 4c. The spectrum for the sample *C* has more intense and narrow peaks at 341, 382 and 413 cm^{-1} (with the strongest peak at 382 cm^{-1}) than the spectrum for the sample *D*. The decrease of the peaks and increase of their width correspond to a decrease in the silicide thickness and crystalline quality or increase in their defect density and concentration of free defects and free carriers that coincide with the blue shift of the plasma reflectance minimum in the reflectance spectrum (Fig. 4b) and low resistivity of $CaSi_2$ layers on Si(111) substrate (sample *E*), which was almost temperature independent [18] and confirmed the high and almost unchanged concentration of free carriers.

An additional intense and wide peak is observed for the sample *D* at 476 cm^{-1} that belongs to amorphous or nanocrystalline silicon (Fig. 4c). Thus, with decreasing $CaSi_2$ layer thickness the crystal quality of silicon capping layer also decreases correlating with HRTEM data for this sample (not shown). Almost the same Raman peaks (344, 390 and 419 cm^{-1}) [18] were observed for the first time for a thick Ca silicide layer (sample *E*) with the initially believed Ca_3Si_4 composition. Meanwhile, the silicide structure and composition are now more precisely determined as hR6-$CaSi_2$ with above mentioned distortion of the lattice (Table 4). Since the peaks at 383 cm^{-1} and 413 cm^{-1} have the highest intensity in DHSs, we can conclude that the formed silicide is conserved without a composition change inside the silicon matrix. The appearance of the strong and narrow peak at 520 cm^{-1} corresponds to the strong contribution from Si crystal, which belongs not only to underlying substrate, but also to the cap layer in the case of the sample *C*.

4.3. Energy band structure, transmittance, reflectivity and adsorption coefficient spectra of $CaSi_2$ by ab initio calculations. Comparison with optical and electrical experimental data

The calculated electron energy band structure of bulk $CaSi_2$ is shown in Fig. 5. It is clearly seen that this silicide should display metallic properties because the Fermi level crosses several bands

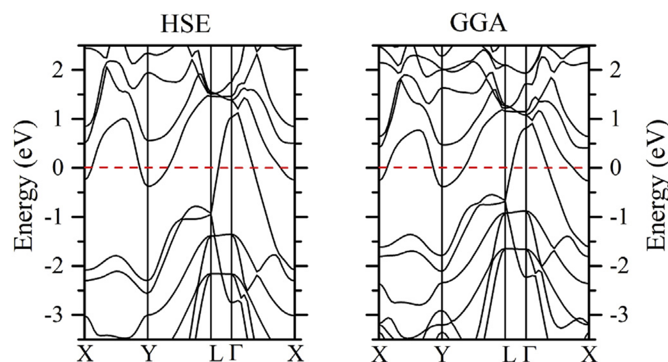

Fig. 5. The electron energy band structure of $CaSi_2$ calculated in HSE (left) and GGA (right) approaches along high symmetry directions of the trigonal Brillouin zone. Zero at the energy scale corresponds to the Fermi level. Symmetry points are X = (1/2, 0, 0), Y = (1/2, 0, 1/2), Γ = (0, 0, 0), L = (1/2, 1/2, 1/2).

regardless of the common GGA (the right panel in Fig. 5) or hybrid HSE (the left panel in Fig. 5) approximations applied. Even though the latter provides better description of the exchange-correlation interaction and can improve predictions of transitions across a gap, there is no significant difference between these two results. One can only spot a shift in energy of bands (filled states go down in energy, while empty states go up in energy) for example in the case of flat bands in the L-Γ segment, which, however, does not exceed 0.5 eV. On the other hand, $CaSi_2$ can be also viewed as a gapless semiconductor. In fact, the valence and conduction bands are separated by the gap, however, the bottom of the conduction band is below the Fermi level (for example at the X and Y points) and top of the valence band stands above the Fermi level (near the Γ point) indicating degenerate semiconducting properties with two types of charge carriers (electrons and holes) in accordance with experimental data [17]. The obtained band dispersion near the Fermi level is close to the one presented in Ref. 13. Because of the lattice mismatch (about 1%) for $CaSi_2$ thin layers grown on Si(111) substrates [12,17] we have also checked how uniaxial strain affects the band dispersion in $CaSi_2$. The applied uniaxial strain of ±3% for both *a* and *c* lattice parameters did not lead to any noticeable changes in the band dispersion presented in Fig. 5.

By means of the full potential linearized augmented plane wave method within the GGA approximation we calculated

transmittance, optical reflectivity and the absorption coefficient for $CaSi_2$ as a function of the photon energy for different light polarizations. They are shown in Fig. 6a-c.

Since $CaSi_2$ is found to be a metal or gapless semiconductor (see Fig. 5), free carrier absorption defines large reflectivity and absorption at low photon energies. However, at 0.7 eV there is a significant drop in reflectivity, whereas the absorption coefficient at 0.7–1.2 eV displays almost zero values (Fig. 6a). To explain such a decrease in the absorption we have examined the character of the states of different bands in the energy range of ±2.5 eV with respect to the Fermi level. The Ca-*d* states are present in this energy range while an admixture of the Ca-*s* and Ca-*p* states are almost negligible. Contrary to this, mainly the Si-*p* and Si-*d* states can be spotted below and above the Fermi level, respectively. Since two Si chemically inequivalent sites exist in the $CaSi_2$ crystal structure, the Si-*p* states of one Si site and the Si-*d* states of another Si site dominate below and above the Fermi level, respectively, at any k-point investigated. Analyzing contributions to the dipole matrix elements and values of dipole matrix elements we can conclude that any matrix element from the Ca site has almost zero value because of a lack of Ca-*s* and Ca-*p* states. Matrix elements coming from the Si sites are also close to zero due to negligible values of one of the contributions from the valence or conduction band assuming only one-site transitions [42]. This feature leads to a transparency window in the $CaSi_2$ optical spectra for photon energies at 0.4–1.0 eV (Fig. 6a). In addition, there is some anisotropy effects in the optical spectra presented in Fig. 6a-c with respect to different light polarizations which are especially pronounced in the energy range of 2.5–5.5 eV.

Recalculated $CaSi_2$ film transmittance, reflectivity and absorption coefficient extracted from experimentally measured transmittance and reflectance spectra, using Kramers-Kronig relations and RT-procedure [41] and their comparison to the theoretically simulated ones are shown in Fig. 6a-c. Multiple reflections and absorption in the film and substrate (a two-layer model), as well as reflection at the film-substrate interface, are considered in the RT procedure [41]. From the data of the experimental reflectance and transmittance spectra in the energy range 0.1–1.2 eV, the refractive index, the extinction coefficient, and the absorption coefficient are determined; first, by solving a system of five nonlinear equations with five unknowns by their consecutive cycle alteration with a variable step, and then by minimizing the deviation of the experimental and recalculated values.

The self-reflectivity coefficient found in this region is cross-linked with the experimental reflectivity spectrum data in the region of interband transitions (above 1.24 eV), which makes it possible to construct a reflection spectrum of the film over the entire energy range up to 6.2 eV. For a $Si/CaSi_2/Si(111)$ double heterostructure, the top layer of silicon and the embedded $CaSi_2$ layer are taken into account as a layer with effective parameters, since in this region of photon energies the main contribution to the absorption is made by a layer of $CaSi_2$. Close values of the reflectivity coefficient from the $CaSi_2$ film and from the double $Si/CaSi_2/Si(111)$ heterostructure with the embedded $CaSi_2$ layer in the constructed spectra (Fig. 6b) prove the validity of this approach. Using the calculated self-reflectivity data for $CaSi_2$ film, their absorption coefficient and thickness, the transmittance of thin $CaSi_2$ layer was recalculated from the two-layer model and experimental data, theoretical optical data and well-known formula for transmittance of thin plane-parallel plate [37]. Thus, the experimental transmittance for $CaSi_2$ layer in two samples C and D and theoretically simulated one for 50-nm thick $CaSi_2$ layer for two light polarizations (E||a и E||c) were presented on Fig. 6a.

The general behavior of both experimental and theoretical transmittances for $CaSi_2$ films (Fig. 6a) in the 0.4–2.0 eV region of photon energies indicate the partial transparency of the $CaSi_2$ layers without a substrate. Certain additional peaks (the sample *C*) of the “experimental” curve at energies of 1.2–1.8 eV are associated with the appearance of multiple reflections in thin layer with partial absorption, which are no longer taken into account in calculations by the Kramers-Kronig method [37]. For the very thin $CaSi_2$ layer in the sample *D*, the transmittance at low energies essentially does not decrease. But for the sample *C*, in which the silicide layer is more than two times thicker (Table 1), the transmittance strongly decreases at photon energies smaller 0.4 eV, which correlates with the absorbance on free carriers in the $CaSi_2$ layer. The same behavior was also observed for the $CaSi_2$ layer calculated from theoretical data. Thus, the small values of the dipole matrix elements of the transitions across the Fermi level of $CaSi_2$ corresponding to small photon energies (0.4–2.0 eV) are responsible for the moderate transparency in the near-IR range.

In the range of strong interband transitions (2.2–6.5 eV) the theoretical results on reflectivity (Fig. 6b) and absorption coefficient (Fig. 6c) should be shifted to the higher photon energies by ~1 eV to have a reasonable agreement with experimental data above 2.2 eV. However, a simple, rigid shift in energy is not straightforward here. Because the HSE calculations are extremely time consuming and there is no significant difference in the energy spectra within the HSE and GGA approximations (Fig. 5) except for the energy shift of 0.5 eV for some parts of bands below and above

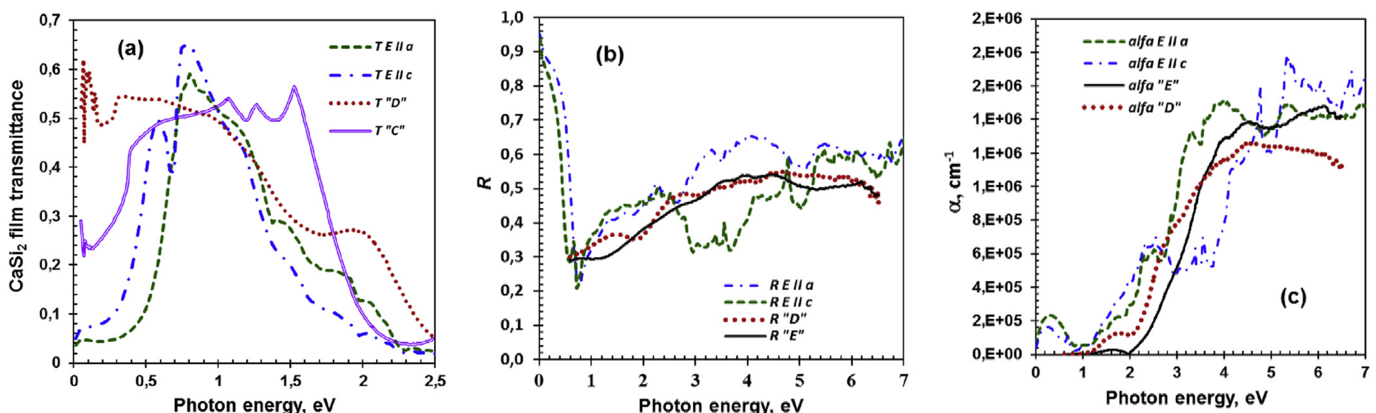

Fig. 6. (a) $CaSi_2$ film transmittance (T) (samples *C* and *D*), (b) reflectivity (R), and (c) absorption coefficient (α) for $CaSi_2$ layers in $Si/CaSi_2/Si(111)$ (sample *D*) and in $CaSi_2/Si(111)$ (sample *E*) in comparison with theoretical data for $CaSi_2$ as calculated within the GGA approximation for different light polarizations ($E||a$ и $E||c$).

the Fermi level, the optical properties have been calculated within the GGA approximation. Thus, by taking into account such an energy shift, the optical spectra can be moved up in energy by ~1 eV, though only starting from 0.7 to 1.0 eV due to the fact that free carrier absorption at lower photon energies is not affected by this energy shift. It is proportional to free carrier concentration and rapidly decreases with photon energy increase. This issue unavoidably increases the transparency window in $CaSi_2$.

In transparent conductive oxides (the most common transparent conductive materials) [43,44], which can be viewed as degenerate semiconductors due to doping, there are always free carriers involved into conduction in addition to absorption and reflection on free carriers at very small photon energies. However, the presence of a rather wide energy gap does not provide any electron transition across the gap for photon energies less than the energy gap leading to no absorption within the infra-red and visible regions and, as a result, to transparency. Contrary, $CaSi_2$ is shown here to be either a gapless degenerate semiconductor or even a metal, where the transparency in the infra-red energy range is attributed to very small values of dipole matrix elements of the transition across the Fermi level.

To establish the nature of conductivity in stressed $CaSi_2$ films on Si(111) substrates, the temperature dependency of the of the direct current Hall effect at a constant magnetic field of B = 0.5 T in the temperature range of 1.4–300 K was studied for the sample *E* (Table 1). The magnetoresistance studies versus a transverse magnetic field were also performed in the sample *E*. In the range of 1.4–25 K, large variations of the calculated parameters (carrier concentration, mobility and resistivity, and magnetoresistance) were observed, therefore, the temperature range of 30–300 K was considered in the following, in which fairly smooth temperature dependences of these parameters were obtained (Fig. 7 (a, b, c)).

Measurements of the Hall and longitudinal voltage biases were carried out at a minimum current of 10 μA to ensure a minimum heating of the film during long-term measurements at each selected temperature. Carrier type measurements (Fig. 7d) showed that there is a rather sharp boundary between the sign of the main carriers and the Hall voltage, which is indicated in the graph by a vertical dashed line. Change from positive to negative occurred at a temperature of more than 85 K (Fig. 7d). Considering the low

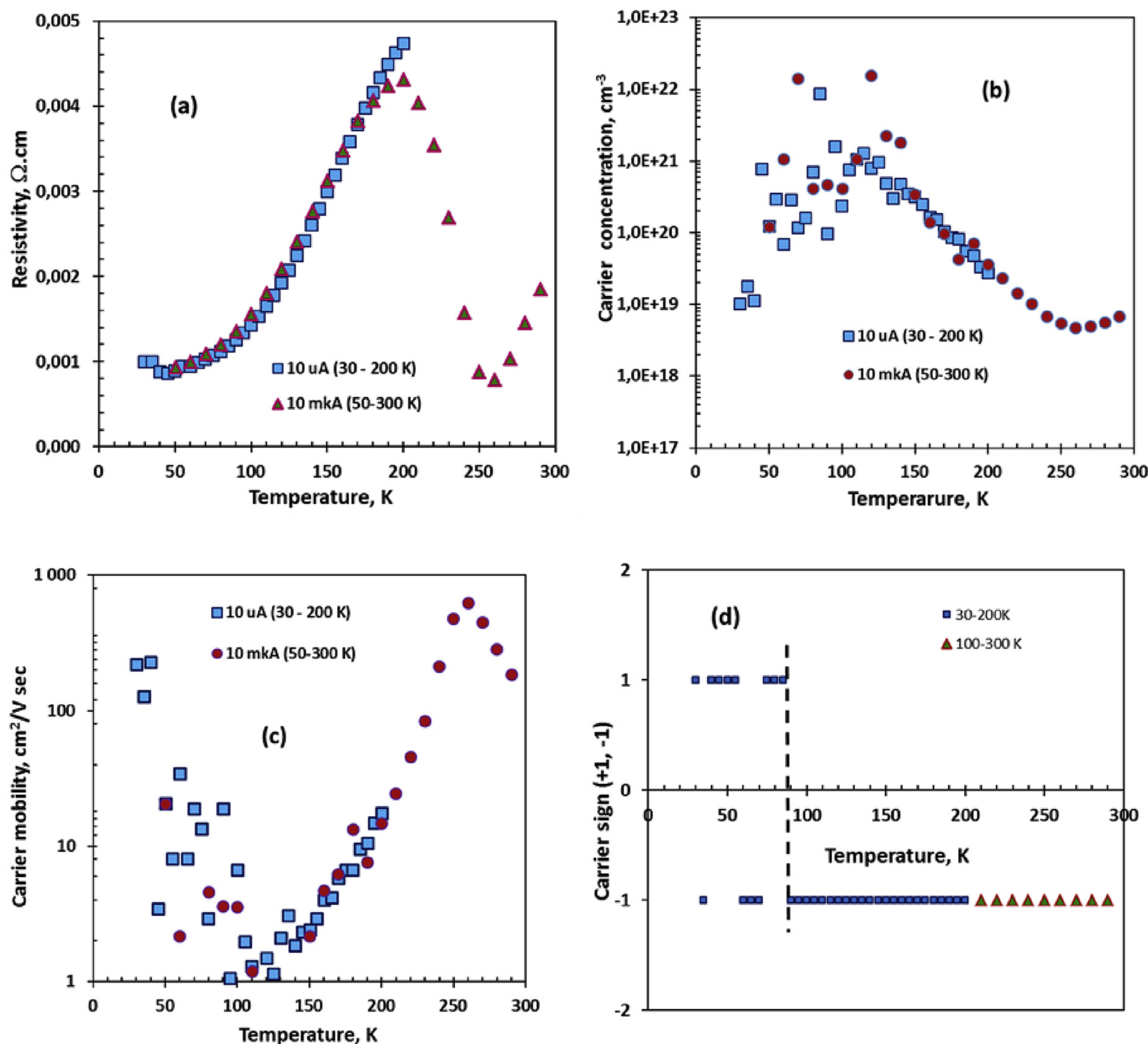

Fig. 7. Temperature dependences of the resistivity (a), the concentration modulus of the main carriers (b), their mobility (c), and the sign of the main carriers (d) in $CaSi_2$ film (sample *E*) grown by the reactive epitaxy on a Si(111) substrate at 500 °C.

temperature and the atypically complex nature of the temperature dependence of the resistivity (Fig. 7a), the carrier concentration (Fig. 7b) and their mobility (Fig. 7c), the observed change in the sign of the main carriers cannot be related to the conductivity type of a gapless degenerate semiconductor at the transition to the region of intrinsic conductivity [45]. The resistivity in the range of 30–200 K did not exceed 5 mΩ × cm and it increased with increasing temperature (Fig. 7a), while in the 200–260 K range it was decreasing, after which it began to rise again. The complex dependences of the concentration of the main carriers and their mobility with maxima and minima in the range from 120 K to 260 K also indicate a non-metal nature of the conductivity.

This behavior can only be explained by assuming the measured sample to be a gapless semiconductor with two "carrier pockets" of different types: both holes and electrons in the valence and conduction bands respectively, which both cross the Fermi level, the position of which varies with increasing temperature from sub-helium to room temperature. Electrons and holes have different effective masses and compete to provide the largest role in conductivity with the increasing temperature due to changes in the volume of "pockets" as can see on Fig. 5a,b. At helium temperatures, the main contribution is made by holes due to the intersection of the Fermi level with a larger "pocket" for holes.

This corresponds to the theoretical calculations that are carried out at 0 K (Fig. 5a,b). Holes provide the main contribution to concentration and mobility, and to the resistivity as well, which tends to fluctuate around a certain constant value in the 30 K vicinity. In the temperature range from 30 to 85 K, the preferential contribution of holes to the conductivity, mobility and concentration is still preserved because the electron concentration is significantly smaller.

With an increase in the temperature from 85 K and higher, the Fermi level apparently moves upward in energy and the volume of the holes "pocket" gets smaller while the electron volume increases. This unavoidably leads to an increase in the contribution of electrons that compete with holes and, as a result, their effective concentration increases, and the mobility decreases. At temperatures above 150 K, the hole concentration decreases strongly, and the electron density stabilizes to a level of 1×10^{19} cm^{-3}. At 260 K the electron mobility reaches a maximum value and then it slightly decreases apparently due to scattering by phonons.

For sample *E*, we also investigated the magnetoresistance in the direction of the magnetic field perpendicular to the flow of current at three temperatures of 50 K, 120 K and 300 K. At 50 K, the magnetic induction dependences of the relative change in the magnetoresistance ($\Delta\rho/\rho$) exhibited strong oscillations (not shown), which did not allow using these data for further analysis. Thus, the values of $\Delta\rho/\rho$ were constructed for 120 K and 300 K From the plot (Fig. 8a) it is evident that both dependences are close to the parabolic shape, characteristic of semiconductors (with two types of carriers) in weak transverse magnetic fields [45]. For the identification of deviations from the parabolic dependence, the dependences of the square of the magnetic induction modulus were constructed (Fig. 8b). It is found that at 120 K two linear sections are observed. At a temperature of 120 K two linear sections are observed. The first linear region ends at about 4.8T^2, which is equivalent to 2.2T. The second starts at the same point with these values, and preserves linearity up to 16 T^2, corresponding to 4 T.

At 300 K, two linear sections can also be distinguished (Fig. 6b), but with a much shorter first section, ending at 1.5T^2 (about 1.2T). The second section has the same slope as the one at 120 K. It can be assumed that they correspond to the same majority carrier type (electrons, from the Hall measurement data (Fig. 5)). In this case it can be assumed that the contribution of holes to the magnetoresistance at a 120 K temperature is still noticeable, but at of 300 K it becomes much less significant, which corresponds to a decrease in the first linear portion along the length. Since the signal $\Delta\rho/\rho$ is proportional to the square of the carrier mobility [45] with the preferential type of carriers (holes or electrons), the hole mobility in $CaSi_2$ is greater than the mobility of the electrons.

Therefore, the grown $CaSi_2$ film on the Si(111) substrate has features of a gap-less semiconductor with two types of carriers that is confirmed by low temperature Hall and magnetoresistance measurements and coincides with the results of our theoretical calculations of the energy band structure of calcium disilicide.

5. Conclusions

Si/$CaSi_2$/Si(111) double heterostructures with thin (14–40 nm) embedded $CaSi_2$ layers were successfully grown by combination of molecular beam epitaxy (MBE) and solid phase epitaxy (SPE) modes of material deposition at the substrate temperature 500 °C. Abrupt epitaxial interfaces were found: $CaSi_2$(001)//Si(111) and $CaSi_2$[−100]//Si [1$\bar{1}$0] with the formation of the embedded thin hR6 $CaSi_2$ crystal in the Si/$CaSi_2$/Si(111) heterostructures. The found epitaxial relations (hR6-$CaSi_2$[100]||Si [1$\bar{1}$0] and hR6-$CaSi_2$(001)||

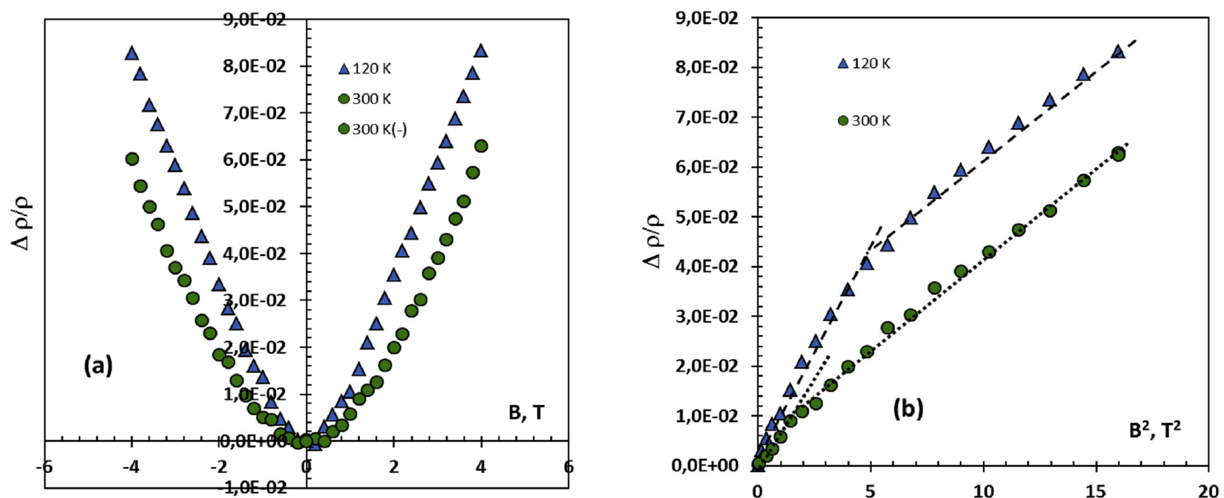

Fig. 8. Dependences of the relative change in the magnetoresistance (from the magnetic induction (a) and the square of the magnetic induction (b) for two temperatures of 120 K and 300 K in a calcium disilicide film (sample *E*).

Si(111)) were conserved for the embedded $CaSi_2$ layers regardless of their thickness in the range from 14 nm to 40 nm independently on the capping Si deposition mode. $CaSi_2$ embedded layers was proven to conserve the compression and stretching with units of percents in the $CaSi_2$ crystalline lattice in different directions. In the Si capping layer of Si/$CaSi_2$/Si(111) heterostructures with $CaSi_2$ thickness of 32–40 nm the {111}-twinned Si crystals were found onto the $CaSi_2$(001) surface and with the {111} planes parallel to the Si(111) of the substrate. A polycrystalline twinned Si capping layer with a variable thickness was formed in the samples with the smallest $CaSi_2$ thickness (14–16 nm).

Optical properties of $CaSi_2$ bulk and a $CaSi_2$ layer embedded into silicon matrix have been studied by theoretical and experimental methods. According to the experimental data a $CaSi_2$ layer displays degenerate semiconductor properties with strong absorbance at the photon energies higher than 2.3 eV and a transparency in the photon energy range of 0.4–1.2 eV. *Ab initio* calculations have predicted $CaSi_2$ to be a metal independently of possible stresses in its lattice, because the Fermi level crosses several bands in the Brillouin zone. On the other hand, $CaSi_2$ can be also viewed as a gapless semiconductor with the Fermi level partial crossing of bottom of the conduction band and top of the valence band in some parts of the Brillouin zone, indicating gapless semiconducting properties with two types of charge carriers (electrons and holes). Low temperature Hall and magnetoresistance versus magnetic field measurements have confirmed a gapless semiconductor nature of $CaSi_2$ film grown by RDE method on the Si(111) substrate. The results of the *ab initio* calculations for different optical functions in comparison with experimental optical data have shown a reasonable agreement in the energy range of 0.8–6.5 eV and an almost complete mismatch at lower energies that can be attributed to the strong absorption due to very high concentration of free carriers in the theoretical model, but which is only partially confirmed by data from Hall measurements, since the hole concentration at 30 K is smaller than $1 \cdot 10^{19}$ cm^{-3}. Thus, $CaSi_2$ is concluded to have simultaneously low electrical resistivity typical for metals and high optical transparency in the near IR-range. Accounting for the simplicity of the method of reactive Ca epitaxy on silicon and moderate temperatures of the process (500^{0}C) for creation of $CaSi_2$, the use of thin $CaSi_2$ layers (50–100 nm) with high transparency in the near-IR range is rather promising for creating conductive contacts to LED structures on silicon with the energy of emitted photons from 0.4 eV to 1.2 eV.

Acknowledgements

This work was carried out with financial support from the Russian Found of Basic Researches grant (No. 16-52-00074) and Belarusian Science Foundation for Fundamental Research (grant No. F16R-048).

References

[1] V.E. Borisenko (Ed.), Semiconducting Silicides, Springer, Berlin, 2000.
[2] K. Maex, M. van Rossum (Eds.), Properties of Metal Silicides, Inspec, London, 1995.
[3] D.B. Migas, V.O. Bogorodz, A.B. Filonov, V.L. Shaposhnikov, V.E. Borisenko, N.G. Galkin, Electronic properties of semiconducting Ca_2Si silicide: from bulk to nanostructures by means of first principles calculations, Jpn. J. Appl. Phys. 54 (1–7) (2015), 07JA03. https://doi.org/10.7567/JJAP.54.07.JA03.
[4] D.B. Migas, V.O. Bogorodz, A.V. Krivosheeva, V.L. Shaposhnikov, A.B. Filonov, V.E. Borisenko, Electronic properties of thin $BaSi_2$ films with different orientations, Jpn. J. Appl. Phys. 56 (1–7) (2017), 05DA03. https://doi.org/10.7567/JJAP.56.05DA03.
[5] D.B. Migas, V.O. Bogorodz, A.B. Filonov, V.E. Borisenko, N.V. Skorodumova, Quasi-2D silicon structures based on ultrathin Me_2Si (Me = Mg, Ca, Sr, Ba) films, Surf. Sci. 670 (2018) 51–57. https://doi.org/10.1016/j.susc.2017.12.017.
[6] D.B. Migas, L. Miglio, V.L. Shaposhnikov, V.E. Borisenko, Comparative study of structural, electronic and optical properties of Ca_2Si, Ca_2Ge, Ca_2Sn and Ca_2Pb, Phys. Rev. B 67 (1–7) (2003), 205203. https://doi.org/10.1103/PhysRevB.67.205203.
[7] S. Lebegue, B. Arnaud, M. Alouani, Calculated particle and optical properties of orthorombic and cubic Ca_2Si, Phys. Rev. B 72 (1–8) (2005), 085103. https://doi.org/10.1103/PhysRevB.72.085103.
[8] D.B. Migas, V.L. Shaposhnikov, A.B. Filonov, N.N. Dorozhkin, V.E. Borisenko, New semiconductor silicide Ca_3Si_4, J. Phys. Condens. Matter 19 (1–8) (2007), 346207. https://doi.org/10.1088/0953-8984/19/34/346207.
[9] P. Manfrinetti, M.L. Fornasini, A. Palenzona, The phase diagram of the Ca-Si system, Intermetallics 8 (2000) 223–228. https://doi.org/10.1016/S0966-9795(99)00112-0.
[10] Z. Yang, D. Shi, B. Wen, R. Melnik, S. Yao, T. Li, First-principle studies of Ca-X (X = Si, Ge, Sn, Pb) intermetallic compounds, J. Solid State Chem. 183 (2010) 136–143. https://doi.org/10.1016/j.jssc.2009.11.007.
[11] S. Fahy, D.R. Hamann, Electronic and structural properties of $CaSi_2$, Phys. Rev. B 41 (1990) 7587–7593. https://doi.org/10.1103/PhysRevB.41.7587.
[12] M. Imai, T. Kikegawa, Phase transitions of alkaline-earth-metal disilicides $M_{AE}Si_2$ (M_{AE} = Ca, Sr, and Ba) at high pressures and high temperatures, Chem. Mater. 15 (2003) 2543–2549. https://doi.org/10.1021/cm0207954.
[13] S.M. Castillo, Z. Tang, A.P. Litvinchuk, A.M. Guloy, Lattice dynamics of the rhombohedral polymorphs of $CaSi_2$, Inorg. Chem. 55 (2016) 10203. https://doi.org/10.1021/acs.inorgchem.6b01399.
[14] J.F. Morar, M. Wittmer, Metallic $CaSi_2$ epitaxial layers on Si(111), Phys. Rev. B 37 (1988) 2618–2623. https://doi.org/10.1103/PhysRevB.37.2618.
[15] G. Vogg, M.S. Brandt, M. Stutzmann, M. Albrecht, From $CaSi_2$ to silixene: epitaxial silicide and sheet polymer layers on silicon, J. Cryst. Growth 203 (1999) 570–581. https://doi.org/10.1016/S0022-0248(99)00135-9.
[16] O. Bisi, L. Braikovich, C. Carbone, I. Lindau, A. Iandelli, G.L. Olcese, A. Palenzona, Chemical bond and electronic states in calcium silicides: theory and comparison with synchrotron-radiation photoemission, Phys. Rev. B 40 (1989) 10194–10199. https://doi.org/10.1103/PhysRevB.40.10194.
[17] M. Affronte, O. Laborde, G.L. Olsece, A. Palenzona, Low temperature properties of calcium mono- and disilicides, J. Alloys Compd. 274 (1998) 68–74. https://doi.org/10.1016/S0925-8388(98)00570-2.
[18] S.A. Dotsenko, K.N. Galkin, D.A. Bezbabnyy, D.L. Goroshko, N.G. Galkin, Formation, optical and electrical properties of a new semiconductor phase of calcium silicide on Si(111), Phys. Proc. 23 (2012) 41–45. https://doi.org/10.1016/j.phpro.2012.01.011.
[19] N.G. Galkin, D.A. Bezbabnyi, K.N. Galkin, S.A. Dotsenko, E. Zielony, R. Kudrawiec, J. Misiewicz, Formation and optical properties of semiconducting thick Ca silicide layers and Si/Ca_xSi/Si heterostructures on Si(111) substrate, Phys. Status Solidi C 10 (2013) 1819–1823. https://doi.org/10.1002/pssc.201300364.
[20] N.G. Galkin, D.A. Bezbabnyi, S.A. Dotsenko, K.N. Galkin, I.M. Chernev, E.A. Chusovitin, P. Nemes-Icze, L. Dozsa, B. Pecz, Solid State Phenom. 213 (2014) 71–79. https://doi.org/10.4028.www.scientific.net/SSP.213.71.
[21] A. Barna, B. Pecz, M. Menyhard, Amorphization and surface morphology development at low-energy ion milling, Ultramicroscopy 70 (1998) 161–171. https://doi.org/10.1016/S0304-3991(97)00120-4.
[22] CrystalMaker Software Ltd, 2016. http://www.crystalmaker.com.
[23] S. Balagan, E. Chusovitin, D. Goroshko, O. Goroshko, Universal algorithm for scanning probe microscopy images grain analysis of objects on the surface, in: 2017 Second Russia and Pacific Conference on Computer Technology and Applications (RPC), 2017, https://doi.org/10.1109/rpc.2017.8168059.
[24] G. Kresse, J. Hafner, *Ab initio* molecular dynamics for liquid metals, Phys. Rev. B 47 (1993) 558. https://doi.org/10.1103/PhysRevB.47.558.
[25] G. Kresse, J. Furthmller, Efficiency of *ab-initio* total energy calculations for metals and semiconductors using a plane-wave basis set, Comput. Mater. Sci. 6 (1996) 15. https://doi.org/10.1016/0927-0256(96)00008-0.
[26] G. Kresse, J. Furthmller, Efficient iterative schemes for *ab initio* total-energy calculations using a plane-wave basis set, Phys. Rev. B 54 (1996) 11169. https://doi.org/10.1103/PhysRevB.54.11169.
[27] G. Kresse, D. Joubert, From ultrasoft pseudopotentials to the projector augmented-wave method, Phys. Rev. B 59 (1999) 1758. https://doi.org/10.1103/PhysRevB.59.1758.
[28] J.P. Perdew, K. Burke, M. Ernzerhof, Generalized gradient approximation made simple, Phys. Rev. Lett. 77 (1996) 3865. https://doi.org/10.1103/PhysRevLett.77.3865.
[29] J. Paier, R. Hirschl, M. Marsman, G. Kresse, The Perdew-Burke-Ernzerhof exchange-correlation functional applied to the G2-1 test set using a plane-wave basis set, J. Chem. Phys. 122 (2005), 234102. https://doi.org/10.1063/1.1926272.
[30] J. Heyd, G.E. Scuseria, M. Ernzerhof, Hybrid functionals based on a screened Coulomb potential, J. Chem. Phys. 118 (2003) 8207. https://doi.org/10.1063/1.1564060.
[31] J. Heyd, G.E. Scuseria, M. Ernzerhof, Erratum: "Hybrid functionals based on a screened Coulomb potential" [, J. Chem. Phys. 118 (2003) 8207, 124 (2006) 219906, https://doi.org/10.1063/1.2204597.
[32] J. Heyd, G.E. Scuseria, Assessment and validation of a screened Coulomb hybrid density functional, J. Chem. Phys. 120 (2004) 7274. https://doi.org/10.1063/1.1668634.
[33] J. Heyd, G.E. Scuseria, Efficient hybrid density functional calculations in solids: assessment of the Heyd-Scuseria-Ernzerhof screened Coulomb hybrid functional, J. Chem. Phys. 121 (2004) 1187. https://doi.org/10.1063/1.1760074.

[34] P. Blaha, K. Schwarz, G.K.H. Madsen, D. Kvasnicka, J. Luitz, WIEN2k, an Augmented Plane Wave + Local Orbitals Program for Calculating Crystal Properties, Karlheinz Schwarz, Tech, Universität Wien, Vienna, 2001.
[35] F. Tran, P. Blaha, Implementation of screened hybrid functionals based on the Yukawa potential within the LAPW basis set, Phys. Rev. B 83 (2011), 235118. https://doi.org/10.1103/PhysRevB.83.235118.
[36] http://www.icdd.com/products/technicalbulletins/Synchrotron_Neutron_Users_Guide.pdf.
[37] J.I. Pankov, Optical Processes in Semiconductors, Dover, New York, 1971.
[38] M.K. Sharov, Plasma resonance in $Pb_{1-x}Ag_xTe$ alloys, Semiconductors 48 (2014) 299. https://doi.org/10.1134/S1063782614030245.
[39] V.I. Ivanov-Omskii, A.S. Mekhtiev, S.A. Rustambekova, E.N. Ukraintsev, Plasma Reflection and hole optical effective mass in p-HgTe, Phys. Status Solidi B 119 (1983) 159. https://doi.org/10.1002/pssb.2221190117.
[40] A.A. Kukharskii, V.K. Subashiev, On the problem of determining the effective mass and time relaxation in semiconductors by the infrared spectrum of light reflection, Semiconductors 4 (1970) 287–293.
[41] N.G. Galkin, A.M. Maslov, A.V. Konchenko, Optical and photospectral properties of $CrSi_2$ A-type epitaxial layers on Si(111), Thin Solid Layers 311 (1997) 230–238. https://doi.org/10.1016/S0040-6090(97)00678-0.
[42] D.B. Migas, L. Miglio, W. Henrion, M. Rebien, F. Marabelli, B.A. Cook, V.L. Shaposhnikov, V.E. Borisenko, Electronic and optical properties of isostructural β-$FeSi_2$ and $OsSi_2$, Phys. Rev. B 64 (2001), 075208. https://doi.org/10.1103/PhysRevB.64.075208.
[43] B.J. Ingram, G.B. Gonzalez, D.R. Kammler, M.I. Bertoni, T.O. Mason, Chemical and structural factors governing transparent conductivity in oxides, J. Electroceram. 13 (2004) 167–175. https://doi.org/10.1007/s10832-004-5094-y.
[44] J. Gao, K. Kempa, M. Giersig, E.M. Akinoglu, B. Han, Ruopeng Li, Physics of transparent conductors, Adv. Phys. 65 (2016) 553–617. https://doi.org/10.1080/00018732.2016.1226804.
[45] Y. Peter, Yu and Manuel Cardona, Fundamentals of Semiconductors, 4 edition, 2000.